Supplementary Information (SI) for ChemComm.

Electronic Supplementary Information

Bismuth incorporation in NiFe hydroxide ultrathin nanosheets boosts methanol electro-upgrading for formate production

Zhuangzhuang Ren,[a,†] Mengping Ren,[a,†] Qianru Wang,[a] Jiaqi Guo,[a] Xu Sun,[b]* Fengcai Lei,[a] Pin Hao,[a] Junfeng Xie [a]*

a Key Laboratory of Molecular and Nano Probes (Ministry of Education), College of Chemistry, Chemical Engineering and Materials Science, Shandong Normal University, Jinan, Shandong, 250014, P. R. China. E-mail: xiejf@sdnu.edu.cn.

b School of Chemistry and Chemical Engineering, University of Jinan, Jinan 250022, Shandong, P. R. China. E-mail: chm_sunx@ujn.edu.cn.

† These authors contributed equally to this work.

S1. Experimental section

S1.1 Chemicals

All chemical reagents were acquired from Sinopharm Chemical Reagent Co., Ltd. and used as received without further purification.

S1.2 Synthesis of Self-Supported Nickel-Iron Hydroxide Catalysts with Controlled Bismuth Incorporation

The 5% bismuth-incorporated NiFe hydroxide nanosheet array (denoted as BNF-5) supported on nickel foam (NF) was synthesized via a one-step solvothermal method. The total concentration of metal ions was maintained at 0.2 mmol, with $Ni(NO_3)_2\cdot 6H_2O$ and $Fe(NO_3)_3\cdot 9H_2O$ employed at a Ni:Fe molar ratio of 4:1. Bismuth nitrate pentahydrate ($Bi(NO_3)_3\cdot 5H_2O$) was added to constitute 5% of the total metal molar content. The designated metal salts, along with 0.6 mmol of urea, were first dissolved in 30 mL of ethylene glycol under continuous stirring for 20 min. Subsequently, 10 mL of deionized water was introduced, and stirring was continued for an additional 10 min to obtain a clear, homogeneous precursor solution. Prior to the synthesis, a piece of nickel foam (4 × 1 cm) was sequentially cleaned by ultrasonication in ethanol for 5 min and then etched in a 1% HCl aqueous solution for another 5 min to remove surface organic residues and oxides, respectively. After thorough rinsing with deionized water and drying, the pretreated NF substrate was immersed into the precursor solution within a 50 mL Teflon-lined stainless-steel autoclave. The autoclave was sealed, heated to and maintained at 200 °C for 12 h, and then allowed to cool naturally to room temperature. The resulting product was collected, washed repeatedly with deionized water and anhydrous ethanol, and finally dried under vacuum at 60 °C for 12 h to yield the BNF-5 catalyst.

For comparison, catalysts with different bismuth contents were prepared by varying the amount of $Bi(NO_3)_3\cdot 5H_2O$ added (0%, 1%, and 10% of the total metal molar amount) while keeping all other synthesis parameters identical. The resulting samples are designated as $NiFe(OH)_x$ (0% Bi), BNF-1 (1% Bi), and BNF-10 (10% Bi).

S1.3 Structural Characterizations

The crystal structure of the synthesized materials was analyzed by X-ray diffraction (XRD) using a Philips X'Pert Pro Super diffractometer with Cu Kα radiation (λ = 1.54178 Å). Morphological examination was performed by scanning electron microscopy (SEM) on a JEOL JSM-6700F microscope. Transmission electron microscopy (TEM), high-resolution TEM (HRTEM), high-angle annular dark-field scanning TEM (HAADF-STEM), and energy-dispersive X-ray spectroscopy (EDS) elemental mapping were conducted using a JEM-2100F and a Thermo Fisher Talos F200X microscope operating at 200 kV. The surface chemical states were investigated by X-ray photoelectron spectroscopy (XPS) on a VGESCALAB MKII spectrometer equipped with an Mg Kα X-ray source (1253.6 eV), with an elemental detection resolution better than 1 at%. The Raman spectra were collected from a laser micro-Raman spectrometer (Horiba LabRAM HR Evolution, 532 nm excitation wavelength). The quantification of liquid products was carried out via ^{1}H nuclear magnetic resonance (NMR) spectroscopy on a Bruker AVANCE 400 MHz spectrometer. For NMR analysis, 500 μL of the post-electrolysis electrolyte was mixed with 100 μL of D_2O, using 0.1 M maleic acid as an internal standard.

S1.4 Methods for Electrocatalytic Measurements

All electrochemical experiments were performed using a standard three-electrode configuration connected to a CHI660E electrochemical workstation. Potentials were measured against a Hg/HgO reference electrode and converted to the reversible hydrogen electrode (RHE) scale. All reported data are presented without iR compensation. A platinum gauze (2 cm × 2 cm, 60 mesh) served as the counter electrode. The as-prepared catalyst on NF, fixed with an electrode holder and connected via a glassy carbon plate, was used directly as the working electrode.

Linear sweep voltammetry (LSV) was conducted at a scan rate of 2 mV s^{-1} in an electrolyte containing 1 M KOH and 0.5 M methanol. Electrochemical impedance spectroscopy (EIS) measurements were performed at 1.35 V vs. RHE over a frequency range from 10^{-2} to 10^5 Hz. The electrochemically active surface area (ECSA) was estimated from the double-layer capacitance (C_{dl}). Cyclic voltammetry (CV) scans were recorded in a non-Faradaic potential window (0.90–1.00 V vs. RHE) at various scan rates (20–100 mV s^{-1}). The C_{dl} value was determined as half the slope of the linear plot of the charging current density difference (Δj at 0.95 V vs. RHE) against the scan rate.

The formate produced during chronoamperometry tests was quantified by ^{1}H NMR. The Faradaic efficiency (FE) for formate was calculated according to the following equation:

$$FE_{formate}\ (\%) = [(n \times F \times c \times V) / Q] \times 100\%$$

where $n = 4$ (number of electrons transferred per formate molecule), F is the Faraday constant (96,485 C mol^{-1}), c is the measured formate concentration (mol L^{-1}), V is the volume of the electrolyte (L), and Q is the total charge passed (C).

S2. Supplementary physical and electrochemical data

The surface chemical states and elemental composition of the catalysts were investigated by X-ray photoelectron spectroscopy (XPS, Fig. S1-S4). As shown in the high-resolution Ni 2p spectra (Fig. S1A, S2A, S3A, and S4A), all samples exhibited characteristic spin-orbit doublets ($2p_{3/2}$ and $2p_{1/2}$) accompanied by satellite features, confirming the coexistence of Ni^{2+} and Ni^{3+} oxidation states.[1] Quantitative analysis revealed a strong correlation between the Bi content and the relative concentration of Ni^{3+} species. Specifically, the proportion of high-valence Ni^{3+} relative to total nickel increased significantly from 18.6% for the undoped $NiFe(OH)_x$ to 34.0% for BNF-5, and further to 42.5% for the heavily doped BNF-10 (Fig. S5). This progressive enrichment of Ni^{3+} with increasing Bi incorporation demonstrates the effective electronic modulation induced by Bi doping. Since Ni^{3+} species are recognized as the catalytically active sites for electro-oxidation reactions, their tunable population is crucial for enhancing the methanol oxidation reaction (MOR) activity.

In the Fe 2p region (Fig. S1B, S2B, S3B and S4B), the dominant peaks were located at binding energies characteristic of Fe^{3+},[2] with no discernible signals corresponding to other valence states, indicating that iron maintained a stable +3 oxidation state in both pristine and Bi-incorporated catalysts.

The high-resolution Bi 4f spectra (Fig. S1C, S3C, and S4C) provided insight into the chemical state of bismuth. For BNF-1 and BNF-5, the primary Bi $4f_{7/2}$ and Bi $4f_{5/2}$ peaks were consistent with the presence of Bi^{3+} species (Fig. S1C and S3C).[3] Interestingly, the spectrum for BNF-10 revealed an additional component at lower binding energy, which can be attributed to the formation of metallic Bi (Fig. S4C). This phenomenon is likely a result of redox interactions with ethylene glycol during the solvothermal synthesis under Bi-rich conditions.[3]

In summary, the XPS analysis confirms that the incorporation of bismuth effectively modifies the electronic structure of the NiFe hydroxide catalyst, primarily by enriching the concentration of electrochemically active Ni^{3+} sites. This electronic regulation, coupled with the lattice disordering observed from structural characterizations, synergistically contributes to the enhanced intrinsic activity toward methanol electro-oxidation.

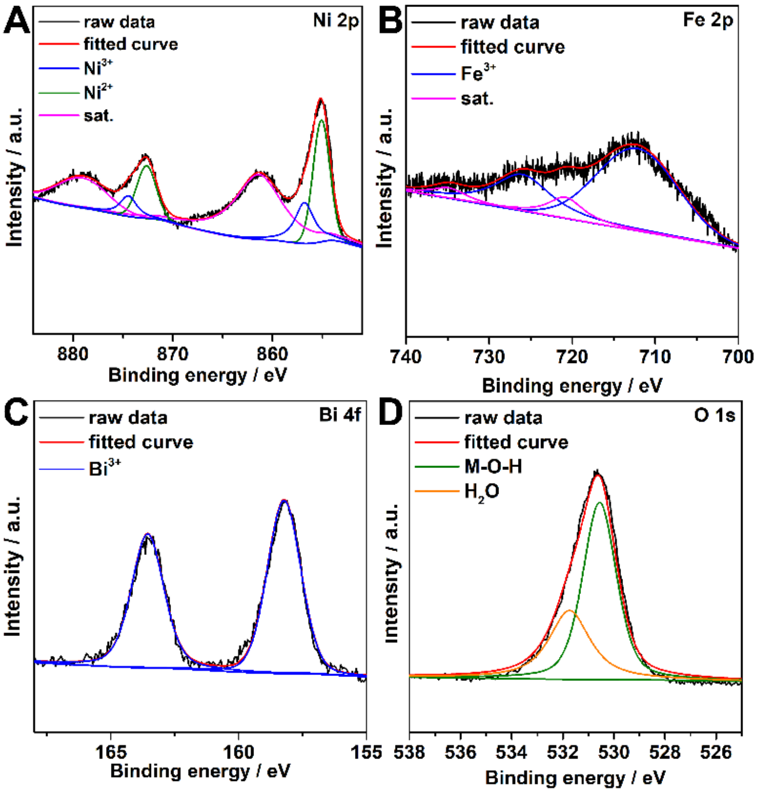

Fig. S1 XPS spectra of BNF-5 for (A) nickel, (B) iron, (C) bismuth and (D) oxygen.

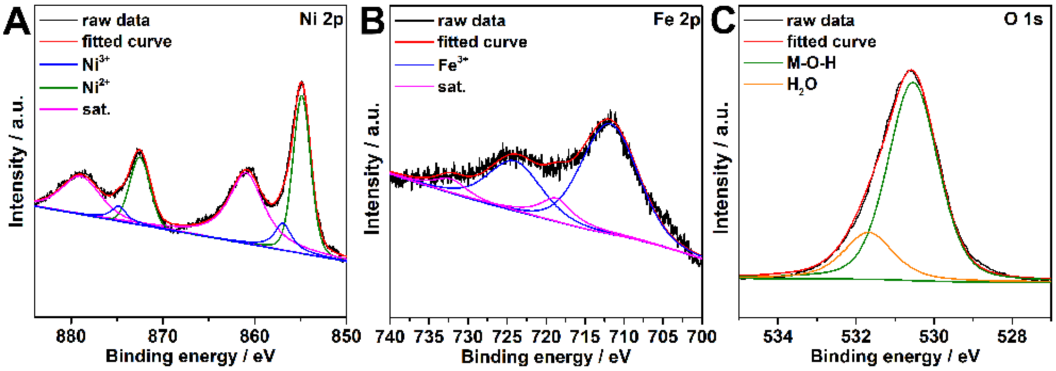

Fig. S2 XPS spectra of NiFe(OH)$_x$ for (A) nickel, (B) iron and (C) oxygen.

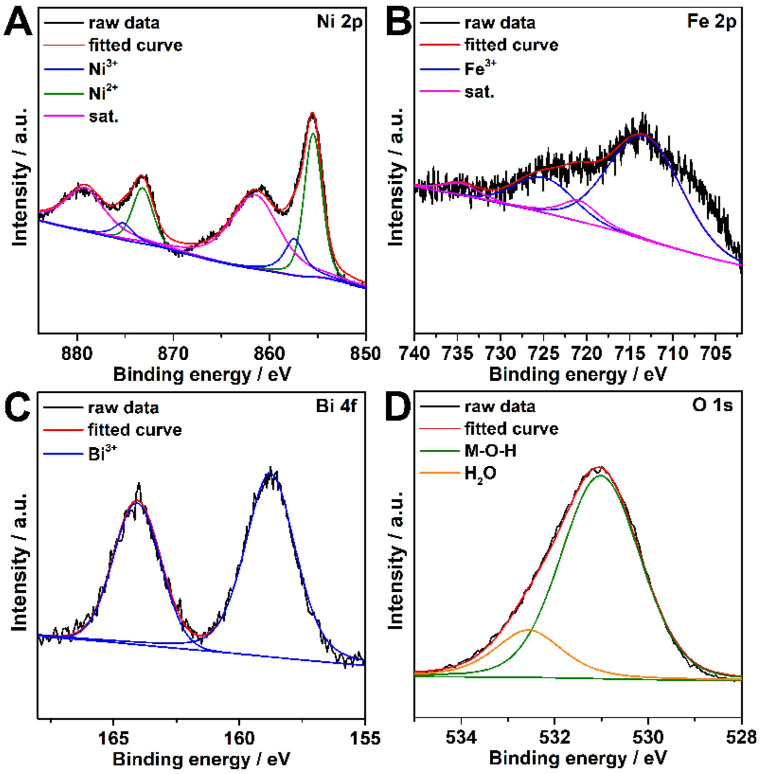

Fig. S3 XPS spectra of BNF-1 for (A) nickel, (B) iron, (C) bismuth and (D) oxygen.

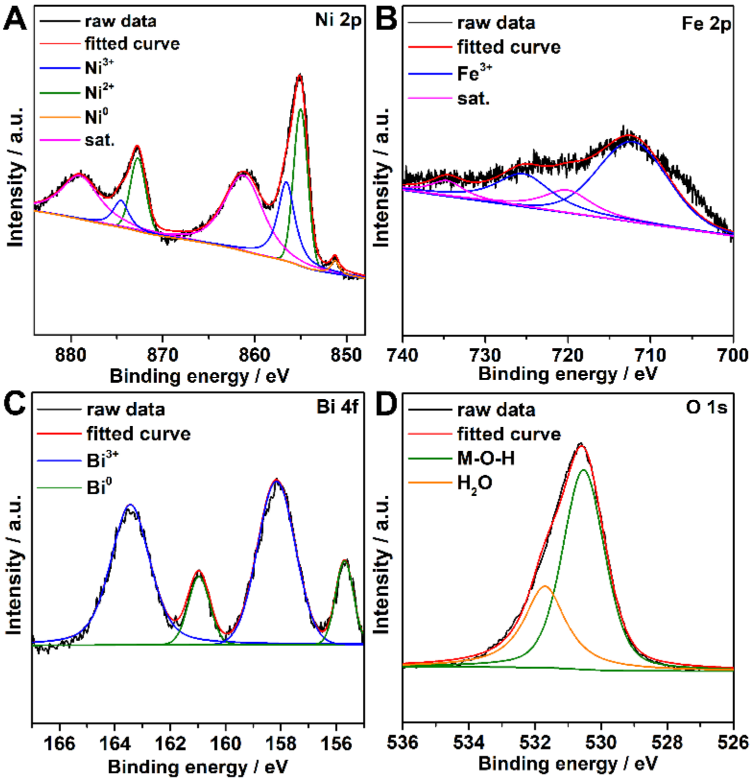

Fig. S4 XPS spectra of BNF-10 for (A) nickel, (B) iron, (C) bismuth and (D) oxygen.

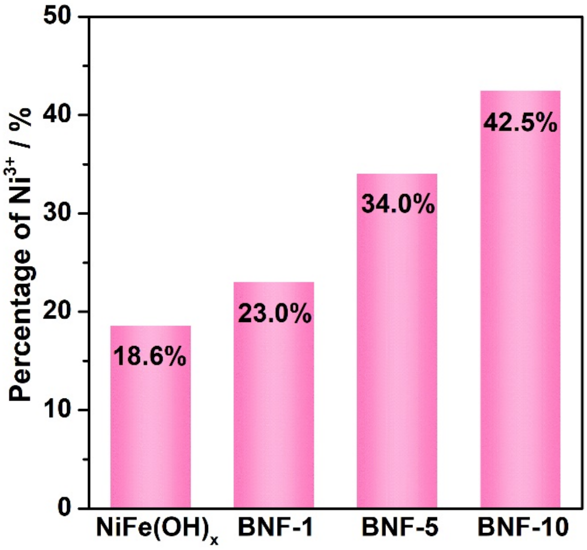

Fig. S5 Percentage of Ni^{3+} species per total Ni for various catalysts. Obvious increment of Ni^{3+} content can be revealed along with increasing concentration of Bi dopant.

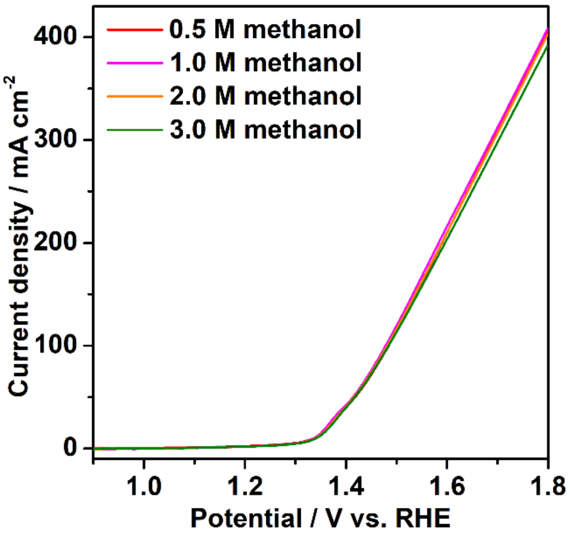

Fig. S6 LSV curves of BNF-5 catalyst in electrolytes with 1.0 M KOH and various concentrations of methanol (0.5–3.0 M).

Table S1. Comparison of MOR performance. Electrolyte: 1 M KOH with varying methanol concentrations as labelled; # indicates that the data were obtained after iR correction; "---" indicates that data were not measured in the cited work; values prefixed with "~" are estimates based on curve analysis and not exact measurements.

Catalysts	C(methanol) [M]	E_{50} [V vs. RHE]	FE [%]	Ref.
BNF-5	**0.5**	**1.375**	**99.9**	**This work**
$NiFe(OH)_x$	0.5	1.440	93.0	This work
BNF-1	0.5	1.423	93.1	This work
BNF-10	0.5	1.456	95.2	This work
NiFe-LDH/NiMo/NF	0.5	1.394	97.0	[4]
$NiFe_xP$@NiCo LDH/CC	0.5	1.400#	~100	[5]
Cu_3N nanosheet	0.5	1.500	>90.0	[6]
Co-N-C/CoO/CF	0.5	1.309	98.2	[7]
ZIF-67/CoO/CF	0.5	1.602	71.0	[7]
CoO/CF	0.5	1.380	84.8	[7]
$Co(OH)_2$/CF	0.5	1.706	87.7	[7]
$Cr_{0.02}Ni(OH)_{2+\delta}$	1.0	1.450	99.8	[8]
Ni_3B/Ni	1.0	1.405	99.9	[9]
Activated NiSn perovskite hydroxide/CC	1.0	1.410	~100	[10]
NiCo PBA	1.0	1.460#	92.5	[11]
Mn-doped NiO	1.0	1.520	97.4	[12]
Fe^{EP}-NiCo-LDH	1.0	1.395	95.0	[13]
Ni-$CuCoN_{0.6}$@CC	1.0	1.400	98.6	[14]
$MoO_3/Ni(OH)_2$	1.0	1.390	---	[15]
Ni-$Bi(OH)_3$/NF	1.0	1.410	>98.0	[16]
Porous Cu@CF	2.0	1.460	---	[17]
$Zn_{0.5}Co$ LDH nanosheet/CF	3.0	1.450	98.0	[18]

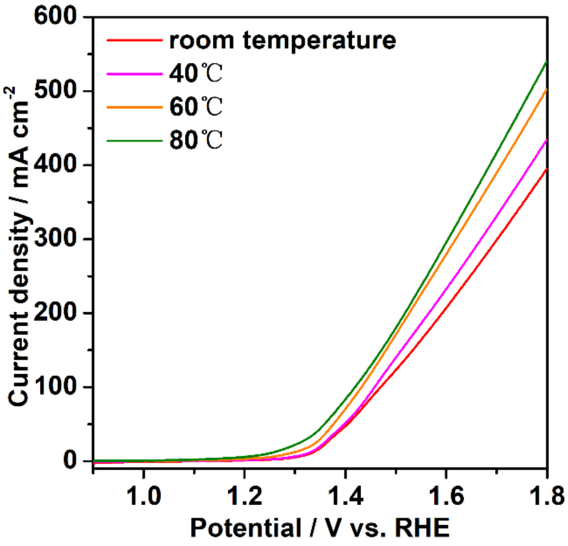

Fig. S7 LSV curves of BNF-5 for MOR at various temperature.

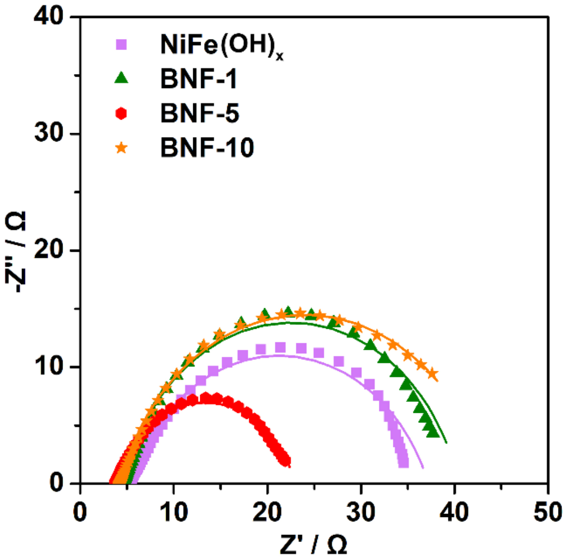

Fig. S8 EIS spectra of various catalysts measured at 1.35 V vs. RHE.

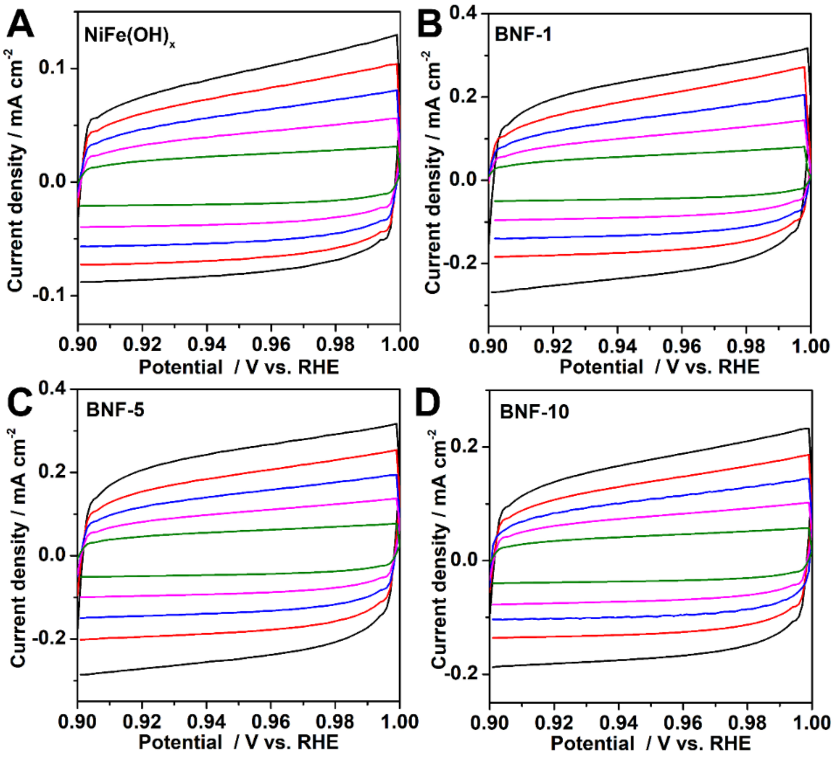

Fig. S9 Cyclic voltammetry curves measured in a non-redox region of 0.9 ~ 1.0 V vs. RHE. (A) Pristine NiFe(OH)$_x$. (B) BNF-1. (C) BNF-5. (D) BNF-10.

The electrochemically active surface area (ECSA) of the catalysts was evaluated using the double-layer capacitance (C_{dl}) method.[19] Cyclic voltammetry (CV) measurements were performed at scan rates ranging from 20 to 100 mV s^{-1} (20, 40, 60, 80, 100 mV s^{-1}) within a non-Faradaic potential window of 0.90 to 1.00 V vs. RHE, where no redox processes occur (Fig. S9). The current response in this region is primarily attributed to double-layer capacitive behavior. The C_{dl} for each catalyst was determined by plotting the current density difference ($\Delta j = |ja - jc|$) at 0.95 V vs. RHE against the corresponding scan rate. The slope of the resulting linear fit is equal to twice the C_{dl} value (Fig. 2D). The calculated C_{dl} values for all catalysts are summarized in Table S2.

Table S2. Calculated C_{dl} and fitted EIS values for each catalyst.

Catalysts	C_{dl} [mF cm^{-2}]	R_s [Ω]	R_{ct} [Ω]
NiFe(OH)$_x$	0.84	5.3	31.9
BNF-1	2.29	4.6	35.8
BNF-5	2.46	3.8	19.2
BNF-10	1.65	4.2	39.4

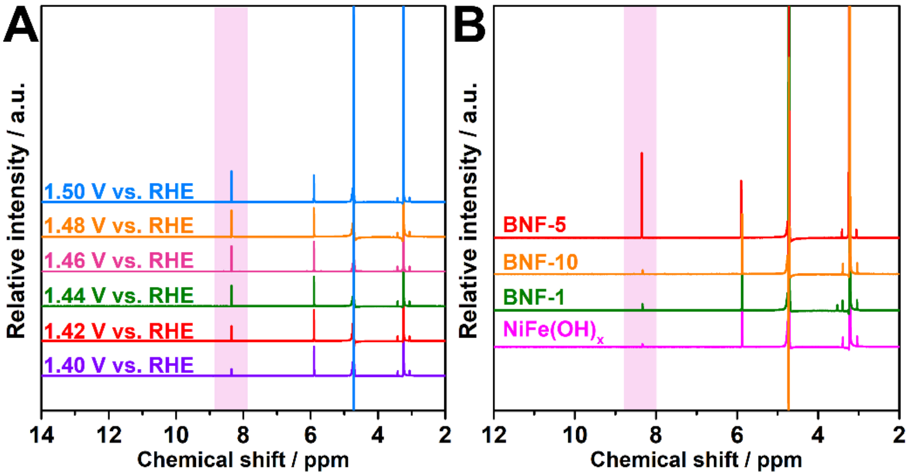

Fig. S10 (A) ^{1}H NMR spectra of the electrolytes obtained at various potentials for 3 h by applying BNF-5 as catalyst. (B) ^{1}H NMR spectra of the electrolytes obtained at 1.42 V vs. RHE for 3 h by applying various catalysts as indicated.

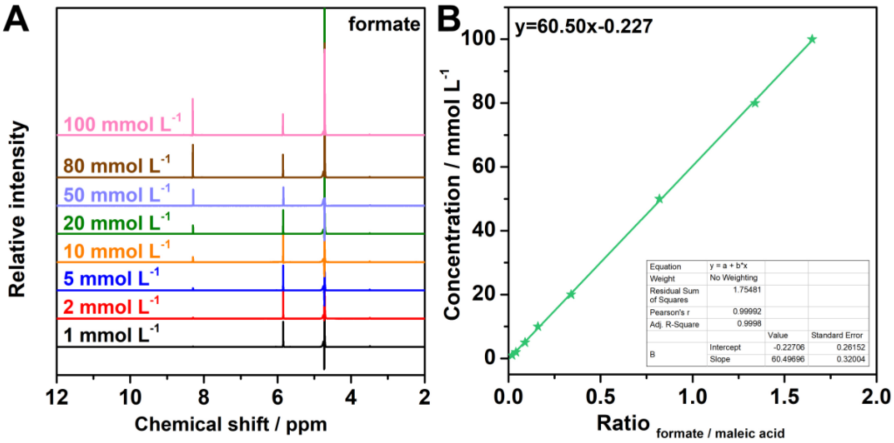

Equation	y = a + b*x		
Weight	No Weighting		
Residual Sum of Squares	1.75481		
Pearson's r	0.99992		
Adj. R-Square	0.9998		
		Value	Standard Error
B	Intercept	-0.22706	0.26152
	Slope	60.49696	0.32004

Fig. S11 ^{1}H NMR spectra of formate solution with standard concentration. (A) Formate is dissolved in 1 M KOH. (B) Standard curve of formate.

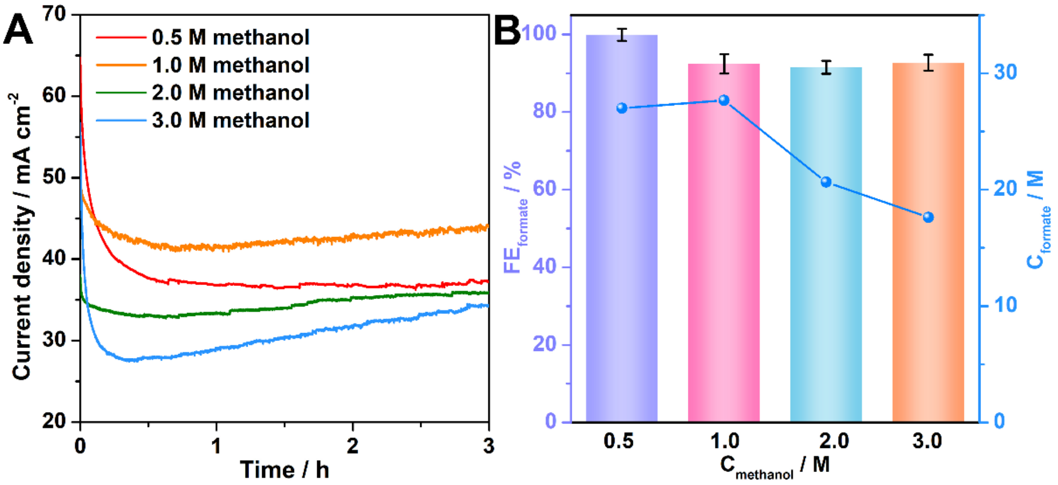

Fig. S12 (A) Chronoamperometry curves of BNF-5 recorded at 1.42 V vs. RHE for 3 h under different methanol concentrations. (B) Corresponding FE of formate and formate concentration as a function of methanol concentration.

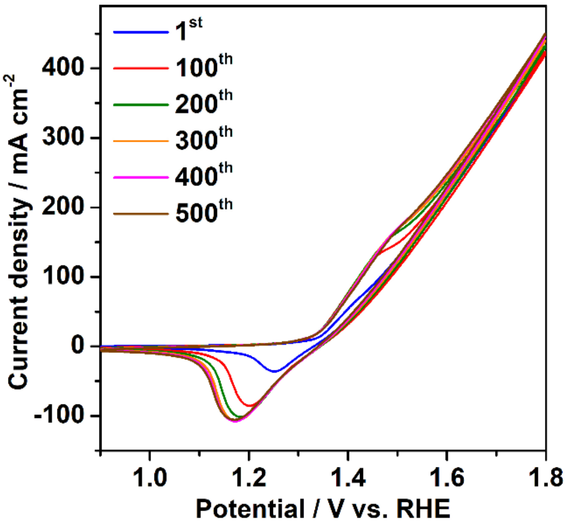

Fig. S13 CV curves of the BNF-5 catalyst at different cycling numbers in 1.0 M KOH + 0.5 M CH_3OH electrolyte.

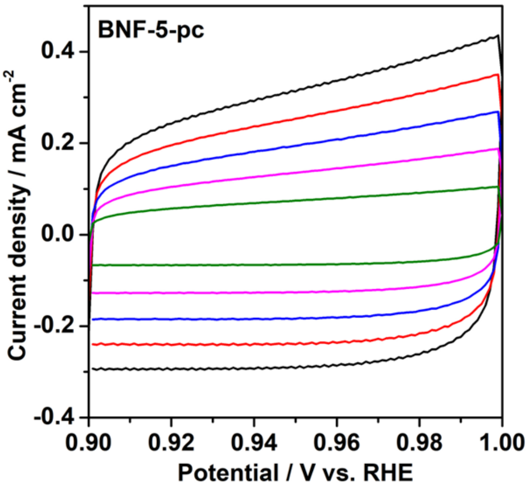

Fig. S14 Cyclic voltammetry curves of BNF-5 after long-term stability test.

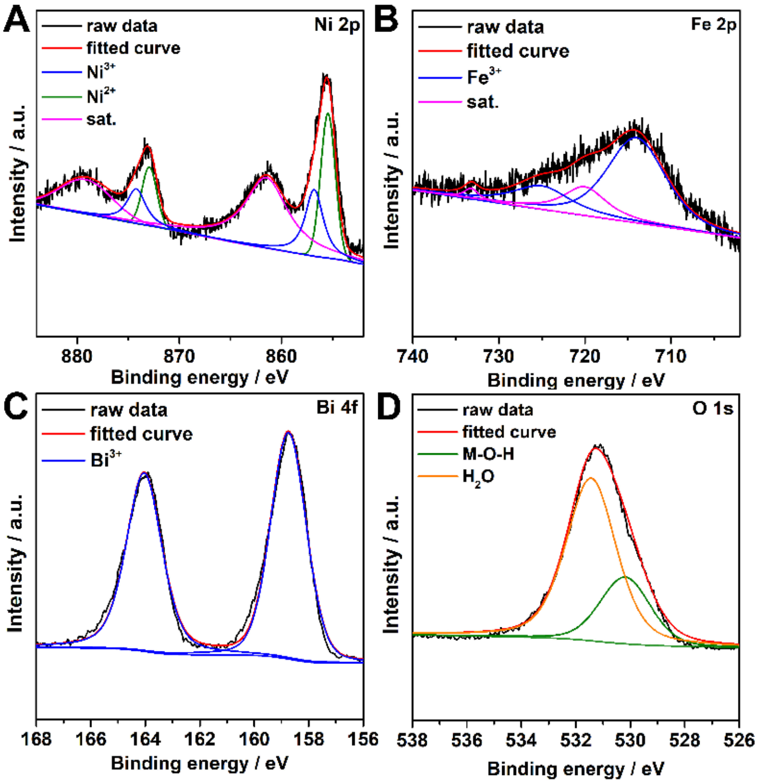

Fig. S15 XPS spectra of BNF-5 after catalysis for (A) nickel, (B) iron, (C) bismuth, and (D) oxygen.

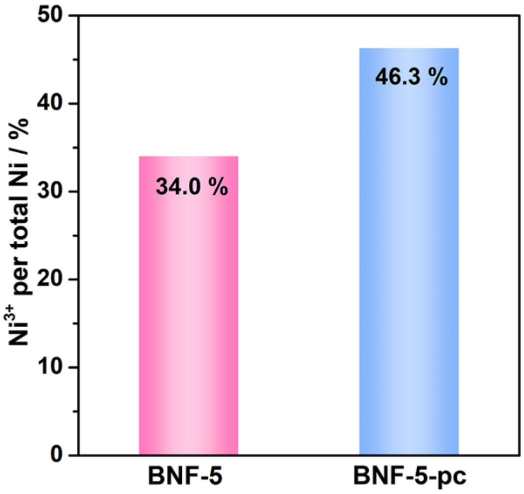

Fig. S16 The proportion of Ni^{3+} in the total nickel metal content before and after stability testing.

To investigate the evolution of the catalyst's surface chemical state after prolonged operation, XPS analysis was performed on the BNF-5 sample following the stability test. In the high-resolution Ni 2p spectrum (Fig. S15A), the peaks centered at binding energies of 855.5 eV and 872.9 eV are assigned to Ni^{2+}, while those at 856.8 eV and 874.2 eV correspond to Ni^{3+}.[1] Notably, a quantitative comparison reveals a significant increase in the relative proportion of Ni^{3+} species after the catalytic reaction compared to the pristine catalyst (Fig. S16). This enrichment of high-valence Ni^{3+}, which are established as active sites for electro-oxidation reactions, is instrumental in facilitating MOR at lower overpotentials, thereby contributing to the enhanced intrinsic MOR activity.[20] The Fe 2p spectrum (Fig. S15B) displays primary peaks at 714.0 eV and 725.0 eV, characteristic of Fe^{3+}, accompanied by satellite features at 720.0 eV and 733.2 eV.[2] Analysis of the Bi 4f region (Fig. S15C) confirms that bismuth retains its +3 oxidation state post-reaction, evidenced by the characteristic doublet at 158.7 eV (Bi $4f_{7/2}$) and 164.0 eV (Bi $4f_{5/2}$).[3] Finally, the O 1s spectrum (Fig. S15D) was deconvoluted into two constituent peaks: the component at 530.2 eV is attributed to metal-hydroxyl (M–O–H) bonds within the catalyst lattice, while the peak at 531.4 eV corresponds to adsorbed water molecules (H_2O) on the surface.[21]

Reference

1. P. Li, J. Zhang, S. Liu, F. Lei, X. Sun and J. Xie, *Chem. Commun.*, 2024, **60**, 9982-9985.
2. X. Yang, L. Kang, Z. Wei, S. Lou, F. Lei, P. Hao, J. Xie and B. Tang, *Chem. Eng. J.*, 2021, **422**, 130139.
3. Z. Ren, R. Wang, X. Pang, W. Zheng, L. Sun, M. Wang, F. Lei, X. Sun and J. Xie, *Nano Res.*, 2025, **18**, 94908017.
4. J. Y. Wang, L. P. Sun, Q. Li, L. H. Huo and H. Zhao, *Mater. Today Chem.*, 2023, **27**, 101338.
5. Y. Zhang, X. Wu, G. Fu, F. Si, X.-Z. Fu and J.-L. Luo, *Int. J. Hydrogen Energy*, 2022, **47**, 17150-17160.
6. L. Zhao, Q. Sun, M. Li, Y. Zhong, P. Shen, Y. Lin and K. Xu, *Sci. China Mater.*, 2023, **66**, 1820-1828.
7. Y. Wang, X. Yang, K. Wang, Z. Liu, X. Sun, J. Chen, S. Liu, X. Sun, J. Xie and B. Tang, *Green Chem.*, 2023, **25**, 8216-8225.
8. H. Qin, Y. Ye, G. Lin, J. Zhang, W. Jia, W. Xia and L. Jiao, *ACS Catal.*, 2024, **14**, 16234-16244.
9. Z. Liu, P. Chang, M. Xi, J. Ding, X. Wang, J. Wang, W. Zhang and Y. Huang, *Small*, 2023, **19**, 2303855.
10. J. Shao, Y. Fang, X. Wu, M. I. Abdullah and Y. Tao, *Nano Res.*, 2024, **17**, 2388-2399.
11. Y. Lin, Y.-g. Wang, X. Li, J. Zhao, H. Liu, C. Wu, L. Yang, G. Li, Z. Qi, L. Shan, Y. Jiang and L. Song, *Small*, 2024, **20**, 2311452.
12. N. Jian, Y. Ma, H. Ge, Y. Zhang, J. Hu, Y. Ke, C. Li, J. Yu, J. Arbiol, J. Liu, A. Cabot and J. Li, *J. Mater. Chem. A*, 2025, **13**, 34772-34781.
13. J. Shi, H. He, S. Zhou, J. Li and W. Cai, *Green Chem.*, 2024, **26**, 2638-2644.
14. F. Jia, Y. Zhang, X. Zhang and T. Hu, *J. Colloid Interface Sci.*, 2025, **677**, 597-607.
15. H. Cheng, B. Dong, Q. Liu and F. Wang, *J. Am. Chem. Soc.*, 2023, **145**, 26858-26862.
16. S. Hao, M. Cong, H. Xu, X. Ding and Y. Gao, *Small*, 2024, **20**, 2307741.
17. F. Zulfiqar, F. Arshad, T. u. Haq and F. Sher, *Int. J. Hydrogen Energy*, 2024, **80**, 1317-1327.
18. S. Jiang, M. Wu, T. Xiao, X. Yin, Q. Gao, C. Xu, M. Zhang, H.-Q. Peng and B. Liu, *ACS Appl. Mater. Interfaces*, 2023, **15**, 55870-55876.
19. J. Xie, J. Zhang, S. Li, F. Grote, X. Zhang, H. Zhang, R. Wang, Y. Lei, B. Pan and Y. Xie, *J. Am. Chem. Soc.*, 2013, **135**, 17881-17888.

20. W. Sun, Z. Wei, J. Qi, L. Kang, J. Li, J. Xie, B. Tang and Y. Xie, *Chin. J. Chem.*, 2021, **39**, 2347-2353.

21. C. Dong, M. Guo, W. Gao, P. Hao, F. Lei, J. Xie and B. Tang, *J. Colloid Interface Sci.*, 2022, **627**, 891-899.